applied sciences

MDPI

Article

Through the Forming Process of Femtosecond-Laser Nanotextured Sheets for Production of Complex 3D Parts

Girolamo Mincuzzi [1,*], Alexandra Bourtereau [1], Laura Gemini [1], Sergi Parareda [2], Sylwia Rzepa [3], Martina Koukolíková [3], Pavel Konopík [3] and Rainer Kling [1]

[1] ALPhANOV, Aquitania Institute of Optics, Rue F. Mitterrand, 33400 Talence, France
[2] EURECAT, Centre Tecnològic de Catalunya, Unit of Metallic and Ceramic Materials, 08243 Manresa, Spain
[3] COMTES FHT a.s., Průmyslová 995, 33441 Dobřany, Czech Republic
* Correspondence: girolamo.mincuzzi@alphanov.com

Abstract: The use of ultra-short pulse lasers in the kW range, combined with an appropriate beam engineering approach, enables the achievement of high-throughput production of laser-functionalised surfaces. However, the manufacturing of complex parts still faces various challenges, such as difficulties in accessing regions with high aspect ratio shapes or intricate profiles, which often leads to the necessity of adapting the laser processing workstation to specific geometries. The forming process is a well-established technique for producing parts of any shape from metallic foils by imposing specific constraints. In this study, we aimed to assess the feasibility of producing laser-functionalised 3D complex products by the forming of laser-treated flat thin metallic sheets. Two-hundred micrometre-thick stainless-steel foils were textured with laser-induced periodic surface structures (LIPSS) through a roll-to-roll pilot line. First, we optimized the morphology of LIPSS. Subsequently, we conducted three types of mechanical tests on both laser-treated and untreated foils: standard tensile tests, fatigue tests, and cruciform specimen tests. We measured and compared parameters such as ultimate tensile strength, breaking strength, maximum elongation, and area reduction between specimens with and without LIPSS, all obtained from the same foil. Additionally, we utilized scanning electron microscopy (SEM) to compare the LIPSS morphology of laser-treated samples before and after mechanical tests.

Keywords: ultra short pulses laser texturing; forming; high-throughput; continous texturing; pre-forming mechanical analysis

Citation: Mincuzzi, G.; Bourtereau, A.; Gemini, L.; Parareda, S.; Rzepa, S.; Koukolíková, M.; Konopík, P.; Kling, R. Through the Forming Process of Femtosecond-Laser Nanotextured Sheets for Production of Complex 3D Parts. *Appl. Sci.* **2023**, *13*, 12500. https://doi.org/10.3390/app132212500

Academic Editor: Antonio Miotello

Received: 3 October 2023
Revised: 6 November 2023
Accepted: 14 November 2023
Published: 20 November 2023

1. Introduction

High-throughput production of large micro- and nanotextured surfaces by laser has been recently reported by different groups [1–6]. It has been achieved thanks to the use of industrial, kW class, ultra-short pulse (USP) lasers jointly with a specific beam engineering strategy [7]. Often, two distinct approaches have been employed: (i) splitting of the beam into several sub-beams by beam shaping techniques to carry out parallel processing [3], and (ii) scanning of the beam at unprecedented speed to mitigate the effects of pulse overlapping [1]. Both approaches made it possible to reduce the takt time of laser texturing down to a few min/m^2. Nonetheless, the high-throughput processing of complex parts is still limited by several issues, such as the difficulty of reaching regions where the geometry of the part exhibits high aspect ratio shapes or tortuous profiles, and the consequent need to adapt the laser processing workstation to the geometry of one part only. To address these issues, post-laser processing techniques can be employed to functionalise large 3D parts, such as, for instance, injection moulding of parts from laser-functionalised moulds. In recent years, this technique has become the method of choice to functionalise some polymeric materials [4,8], but efforts still need to be put in place to extend the process to a larger range of polymers and other materials like metals.

The forming process is a well-known method for producing parts of any shape from metallic foils by applying specific constraints. It could represent an attractive solution for the generation of 3D laser-functionalised shapes compatible with mass industrial production. However, for most applications [9,10], it is important that after the laser texturing, the flat metallic surface retains unchanged mechanical characteristics and eventually its surface properties.

In this work, the forming of 200 μm thick USP laser nanotextured stainless-steel foils and the mechanical properties of the final formed functionalised parts were investigated to evaluate the possibility of employing this post laser-processing technique to produce laser-functionalised 3D complex products. Furthermore, the potential for using forming to generate 3D functionalised shapes at an industrial scale depends on the mass production of textured surfaces that can be subsequently shaped. In this study, we utilized a laser processing workstation based on a roll-to-roll design, allowing for continuous treatment of parts. The setup included a high-power, MHz, USP laser (max P = 320 W) and a fast polygon scanner to prevent heat accumulation phenomena. It made it possible to process coils as long as several tens of meters with a cycle time as short as 5 min per square meter, depending on the required surface texture [11]. Initially, laser-induced surface morphologies were optimized to achieve the highest level of morphological homogeneity and uniformity, free from unwanted thermal effects. This allowed neglecting a possible dependence of the mechanical test results on the surface imperfections. Once the laser process parameters were identified, a 200 μm thick stainless steel foil was textured by generating highly homogeneous laser-induced periodic surface structures (LIPSS). Several specimens were finally cut from untreated, and laser-treated foils and subjected to a comprehensive set of mechanical tests (both static and dynamic) simulating the conditions a metallic foil undergoes during the forming process. A comparative study has been conducted (nanotextured vs. untreated) to highlight the impact of nanotexturing on the forming process and gain insights into its feasibility.

2. Materials and Methods

2.1. Laser Processing Workstation

A linearly polarised, 450 fs, λ = 1030 nm, laser source delivering a maximum average power P = 310 W with maximum repetition rate RR = 13 MHz (Tangor, by Amplitude Laser, Pessac, France) was utilised to generate nanometric laser-induced periodic surface structures (LIPSS) on the surface of a 200 μm thick, 304 stainless-steel coil (see Figure 1). The coil width was 40 cm. Estimations of the surface roughness value S_a were obtained by means of the software ConfoMap ST 8.2 after surface profile acquisitions carried out with a ×50 optical profilometer (Smart Proof 5, by Zeiss, Göttingen, Grmany). The laser beam was magnified by a factor of 2, then deflected by a hybrid polygonal galvanometric scanning head (UHSS-II-15, by Raylase, Wessling, Germany) and focused through an F-theta lens with focal length f = 650 mm. This system enables scanning speeds as high as 360 m/s with a scanning field ≥350 mm. The coil is automatically unwrapped through a motorised rotator, then pulled for nearly 1.5 m through a second rotator. Before reeling, the coil passes beneath the laser beam. The web tension can be adjusted between 10 MPa and 100 MPa, and the line speed v_l can vary between 3 mm/s and 20 mm/s. Amongst the metallic sheets (Al, Ti, Mg alloys, etc.) which are commonly subjected to forming [12], we chose stainless steel since it has been widely studied in USP laser nanotexturing [13]. The chosen thickness value was the maximum compatible with our set-up. Handling of thicker coils will require the implementation of more powerful motorised rotators.

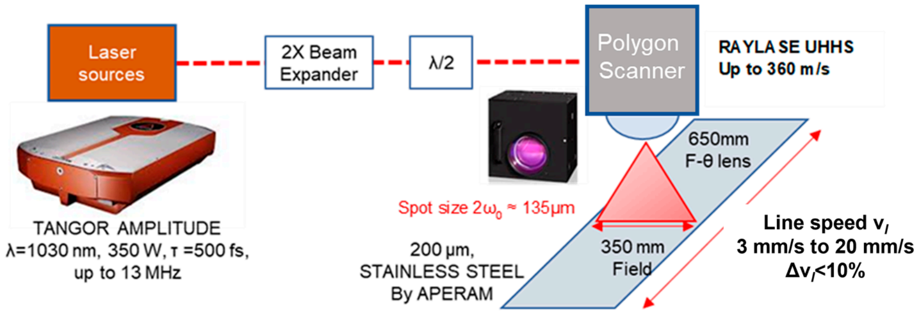

Figure 1. A schematic of the R2R pilot line.

2.2. Mechanical Testing Procedures

Three types of mechanical resistance tests were carried out on laser-treated and untreated 200 µm thick stainless-steel foils: standard tensile tests (i), fatigue tests (ii) and cruciform specimen tests (iii). Tensile tests (i) were performed using specimens shown in Figure 2a to evaluate basic mechanical parameters (yield strength YS, ultimate tensile strength UTS, uniform elongation UE, total plastic elongation EL and reduction of area RA) and the material's anisotropy.

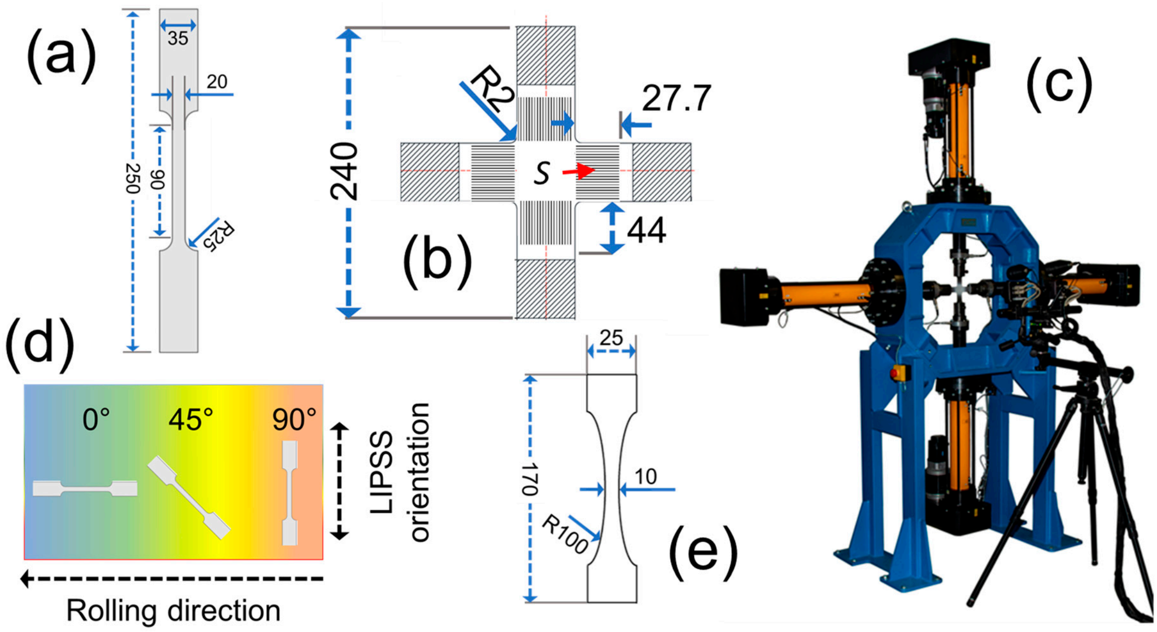

Figure 2. (**a**) Specimen geometry for standard tensile testing; (**b**) cruciform specimen geometry dedicated for the mechanical testing performed in three loading modes (plane strain, uniaxial and biaxial); distance between slits *S* was 300 µm; (**c**) cruciform specimen testing setup equipped with a Digital Image Correlation system for deformation tracking; (**d**) direction of cutting for specimens in three different directions with respect to LIPSS orientation; (**e**) hourglass specimens for the fatigue tests. All values are given in mm.

For the latter, three specimens were cut from the untreated and laser-treated foils in three different directions β with respect to the rolling orientation (see Figure 2d): β = 0° (perpendicular to LIPSS direction), β = 45° and β = 90° (parallel to LIPSS direction). The tests were performed under quasi-static conditions at room temperature according to standard procedures reported in [14]. For the sake of repeatability, each test was carried out in the same conditions three times using a Mayes universal testing machine (designed and developed in house by COMTES, Dobřany, Czech Republic) equipped with hydraulic grips and a crosshead velocity of 1.2 mm/s.

The fatigue strength (ii) was evaluated in the high cycle fatigue (HCF) regime, following the recommendations reported in [15]. At least 10 hourglass specimens with a stress concentration factor (K_t) of 1.02 (Figure 2e) machined in the β = 90° direction were tested for each condition. The tests were conducted at room temperature using a servo-hydraulic testing machine (Landmark by MTS, Berlin, Germany) equipped with a 1 kN load cell and mechanical grips. A load frequency of 30 Hz was applied, and the stress ratio (R = Min stress/Max stress) was set at 0.1 to prevent specimen buckling. The fatigue limit was defined at 2 million cycles.

The tests (iii) performed using cruciform specimens (see Figure 2b) were carried out to investigate the effect of different pre-strain conditions on both untreated and laser-treated foils. Three different loading modes were applied to pre-strain the specimens: plane strain (zero strain in the direction perpendicular to loading), uniaxial (loading applied in one direction) and biaxial (loading applied in two directions) tension. Each specimen was firstly tested until failure (designated as 100%), then pre-strained at 75%, 50% and 25% of the failure elongation. Figure 2c illustrates the testing setup for cruciform specimens equipped with a digital image correlation (DIC) system for tracking deformations. Finally, samples of tests (iii) were characterised via SEM.

3. Results and Discussion

3.1. Optimisation of LIPSS Morphology

Nanometric LIPSS are currently being evaluated to produce next-generation advanced materials in a wide range of application sectors, such as the biomedical, aerospace, automotive, food-handling, home-appliance industries, and so on [16–18]. The generation of LIPSS over surfaces much larger than the spot size (>>1 cm^2) is normally achieved by the raster scanning technique. In this case, large-scale LIPSS homogeneity is linked to the laser process parameters, mainly the energy dose Φ and the laser beam polarisation orientation [19]. Φ corresponds to the cumulative energy deposited on the unit of irradiated surface (J/cm^2) and takes into consideration key parameters such as the energy per pulse E, the repetition rate RR and the spatial overlap between successive pulses, which in turn play a role in thermal accumulation phenomena [1]. In order to define a set of laser process parameters where LIPSS are generated uniformly, the energy dose Φ was fixed at 0.55 kJ/cm^2 and the scan speed at 90 m/s coherently with results reported for similar experimental conditions [1]. Moreover, to maximise the throughput, the average power P was kept constant at 260 W (i.e., the maximum available on the stainless-steel coil after optical losses), and RR was varied in the range of 1–10 MHz, corresponding to E varying from 26 μJ to 260 μJ, respectively. Laser-treated surface morphologies were finally analysed by SEM (Vega3, by Tescan, Brno, Czech Republic). Figure 3 presents SEM images of the laser-treated surfaces, and for each image, the insets show the respective FFT analyses. The yellow arrows represent the orientation of the laser beam polarisation on the irradiated surface. Starting from relatively low RR (RR = 1 MHz and RR = 2 MHz) the LIPSS morphology was irregular and not well-defined. In these cases, the corresponding E (respectively, E = 260 μJ and E = 130 μJ) was too high, leading to important ablation phenomena and preventing the generation of uniform structures. Increasing RR, E decreased, and structures became more regular. An optimum appeared in correspondence with RR = 5 MHz and E = 52 μJ s. Further increasing RR, the E decreased proportionally, and the observed morphology underwent a slight degradation. Similar results have been already reported in the literature for Steel [20,21] and ascribed to the increase in the spatial overlapping between two successive pulses. In fact, this led to an extension of the surface where the surface plasmon polaritons generated by the second pulse interacted with the pattern generated by the first, thus decreasing the pattern regularity.

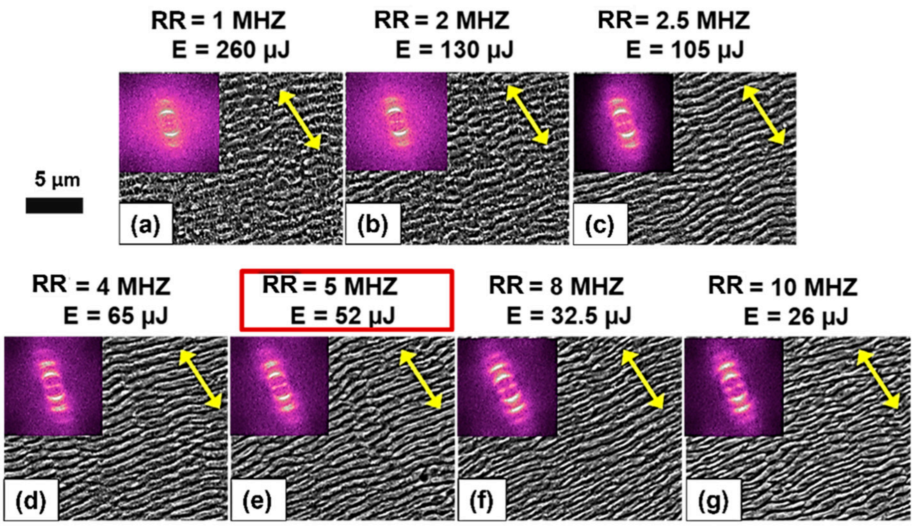

Figure 3. SEM images and related FFT analyses of LIPSS generated by different sets of parameters couples (RR, E): (1 MHz, 260 µJ) (**a**), (2 MHz, 130 µJ) (**b**), (2.5 MHz, 105 µJ) (**c**), (4 MHz, 65 µJ) (**d**), (5 MHz, 52 µJ) (**e**), (8 MHz, 32.5 µJ) (**f**), (10 MHz, 26 µJ) (**g**). In the red box are highlighted the optimum parameters values.

Our trend was confirmed by the FFT analysis, which made it possible not only to extract the LIPSS period value but also the angular dispersion θ of the FFT peak. The latter represents an effective and quantitative evaluation of the LIPSS homogeneity [22]: the lower the θ, the higher the structure's homogeneity.

As shown in Table 1, a minimum was observed for RR = 5 MHz and E = 52 µJ, where θ = 11°. This value is consistent with those previously reported in the literature [20,22]. Finally, we observed that the same experimental approach could be used to extend the above-mentioned results to sheets of metals like Ti, Mo, Ni, Al, Cu, etc. It is worth observing that although for Ti and Mo, we can expect an optimum θ value of roughly between 5° and 10°, for Al, Ni and Cu, it will be much higher, given that the values reported in the literature ranged between 20° and 30° [20].

Table 1. Spatial period (Λ) of LIPSS and angular dispersion (θ) obtained by FFT analyses. The selected parameters are highlighted in bold.

E (µJ)	Λ (µm)	θ (°)
260	889	24
130	837	22
105	835	21
65	837	15
52	**819**	**11**
32.5	839	16
26	822	18

3.2. Influence of Laser Treatment on Mechanical Properties

A set of laser processing parameters, of E = 52 µJ, RR = 5 MHz, scan speed = 90 m/s, and v_l = 3 mm/s, was selected to functionalise a 2 m long coil for the successive mechanical resistance tests.

3.2.1. Tensile-Stress Analyses

Figure 4 shows the variation in the measured engineering stress (MPa) vs. the engineering strain for laser-treated (a) and untreated (b) specimens, with β = 0° (i.e., 90° with respect to LIPSS direction, green points), β = 45° (blue points) and β = 90° (orange, yellow and red points, same direction as LIPSS orientation). Except for "β = 0°, laser treated", three different samples were fabricated and tested for each condition. It can be observed that all specimens showed the same trend with comparable values, with a stabilization of the stress values in the range of 600–700 MPa for strains above 30%.

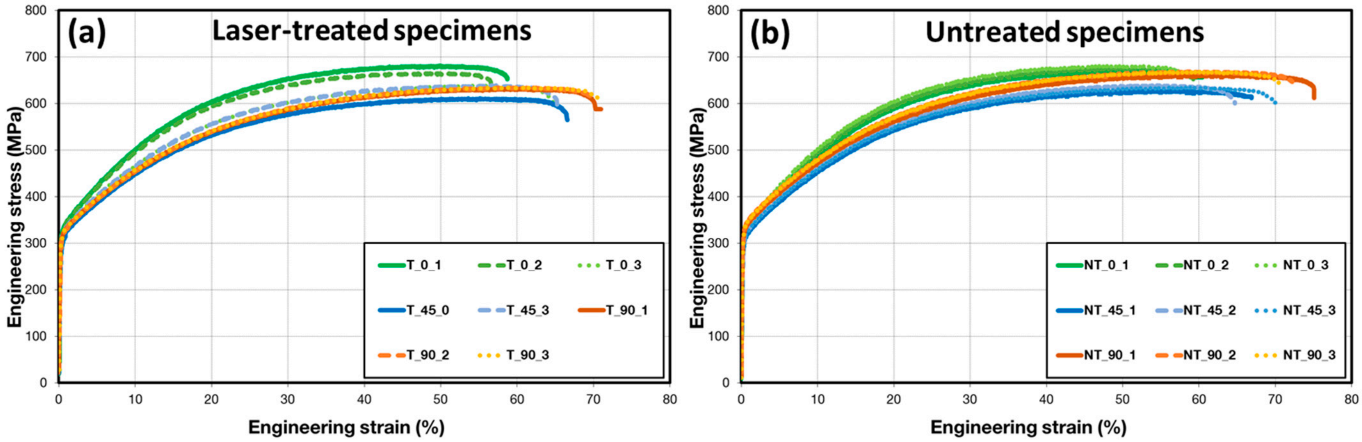

Figure 4. Results of standard tensile test—engineering stress vs. engineering strain diagrams of representative specimens cut from (**a**) untreated and (**b**) laser-treated sheets; designation system in the legend: T/NT—laser-treated/untreated, 0/45/90—specimen orientation with respect to the rolling direction of metal sheet. For laser-treated samples, specimens cut at 90° represent specimens where the strength is applied in the same direction as the LIPSS orientation.

Figure 5 summarises the average values obtained for key mechanical parameters like YS (orange bars), UTS (blue bars) (see Figure 5 left), UE (orange bars), EL (blue bars) (see Figure 5 centre), and RA (blue bars) (see Figure 5 right). YS expresses the limit of the elastic behaviour of the material and identifies the stress value at the beginning of plastic behaviour. The UTS defines the maximum stress the material can withstand. Both are expressed in MPa (force/area). UE is the value of elongation in correspondence of UTS. EL corresponds to the value of strain at the material break (excluding the elastic part of the stress–strain curve). RA is a ratio of minimal and original cross-sections of the same specimen during the test. UE, EL and RA values are expressed in %. For each graph in Figure 5, values relative to the laser-textured batch (T) are plotted on the left side whilst those relative to untreated specimens (NT) are plotted on the right side. It is easy to observe that values relative to the two batches (T) and (NT) are largely compatible if not equivalent when considering the error bars. This means that the surface texturing generated using nearly P = 260 W has no impact on the mechanical properties of the foil. This can be explained considering two key aspects. On one hand, the use of a fast polygon scanner prevents heat accumulation phenomena and unwanted thermo-mechanical degradations (see SEM analysis below) expected also for fs laser when considering high RR (MHz) and high P values [23,24]. On the other hand, although the variation in S_a has a bearing on the mechanical properties of a metallic sheet [25], in our case the S_a contribution induced by LIPSS could be neglected. In fact, we estimated a value of S_a = 253 nm for the pristine foil and S_a = 272 after the texturing, corresponding to a relative variation of ≈7%.

Going in deeper, Figure 5 (left) shows that both strength values (YS and UTS) were not affected by the value of β (specimen orientation). On the contrary, elongation parameters (Figure 5 centre and right) like UE and EL increased when β passed from 0° to 90°. As already mentioned here below, this anisotropic behaviour is not related to laser texturing. Very likely, it is related to both the thermal and mechanical processes the steel undergoes before reaching the shape of 200 µm thick foil. For instance, the rolling process required to reduce the foil thickness and manufacture the coil increases the stiffness along the rolling direction (β = 0°), with the possibility of reducing the values of elongation parameters [26].

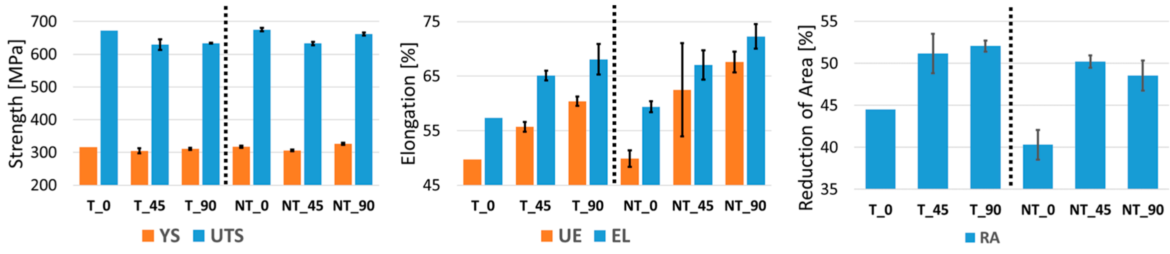

(a) (b) (c)

Figure 5. Results of tensile stress tests carried out on laser-treated (T) and untreated (NT) specimens in different cutting directions. (**a**) Yield strength (YS) and ultimate tensile strength (UTS), (**b**) uniform elongation (UE) and total plastic deformation (EL), and (**c**) reduction of area (RA). Error bars represent standard deviation values.

3.2.2. Fatigue Test Analyses

Figure 6 shows the S–N or Wöhler curve, i.e., the maximum stress (S) versus the number of cycles to fracture (N) for both untreated (circles) and laser-textured specimens (triangles). It is worth noting that laser-textured and untreated specimens showed the same fatigue resistance, reporting the same fatigue limit at 516 ± 6 MPa, fatigue strength coefficient σ'_f and fatigue strength exponent b of the Basquin stress–life relation as reported in Table 2.

Table 2. Basquin stress–life parameters for each surface condition.

Surface Condition	σ'_f (MPa)	b
Untreated	730	0.024
Laser-treated	734	0.025

To understand this result, one should consider the generally accepted correlation between fatigue resistance and surface state. A rough surface with deep defects could decrease the fatigue resistance of a material, especially at a cycle regime as high as around 10^6 cycles [27]. In fact, defects or surface valleys act as stress raisers, leading to the initiation of fatigue cracks and compromising the material's resistance to fatigue [28]. The larger the size of the defects or the depth of surface valleys, the higher the impact of the mentioned mechanism. In our case, we can consider that LIPSS have a period of 800–900 nm and typical height of 150–250 nm [29]. These values are significantly lower than the critical crack length ($\sqrt{area}_{critical}$) of 8 µm, calculated according to Yang et al. [30].

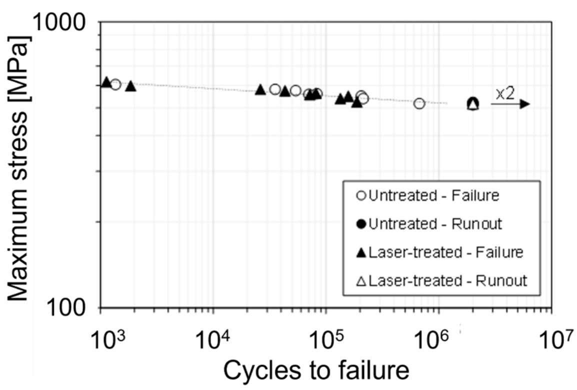

Figure 6. Results of fatigue tests carried out on laser-treated and untreated specimens. The arrow indicates the number of specimens that reached the runout.

3.2.3. SEM and Cruciform Tests Analyses

Cruciform specimens shown in Figure 2b were obtained from laser textured foil and then subjected to an increasing load until the failure was reached (hereinafter 100%). This test was carried out in three different conditions, i.e., applying the load along a single axis (uniaxial, UNI), along two perpendicular axes (biaxial, BI) and with a plane strain loading (PS). To validate the resilience of LIPSS and consequently of the surface functionality after a forming process, SEM analyses were carried out on a textured specimen before and after the tests.

Although a slight reduction in the LIPSS height might be expected [31], the results shown in Figure 7 indicate that the LIPSS morphology was not affected by the mechanical load, regardless of the direction along which the load is applied. The morphology observed before the tests (Figure 7 left) was kept unchanged not only at 100% but also for specimens subjected to a load (pre-strain) value, enabling an elongation of, respectively, 75%, 50% and 25% of the failure (micrographs not shown).

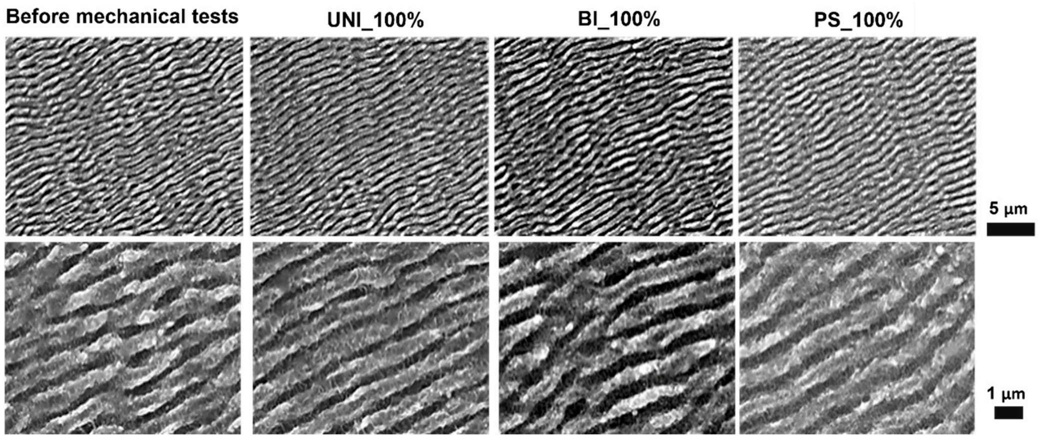

Figure 7. SEM images of laser-treated surfaces after cruciform tests. Loading modes: BI: biaxial tension, UNI: uniaxial tension, PS: plane strain.

4. Conclusions

For the first time, we report a successful demonstration of the continuous manufacturing of laser-induced nano-textured foils using a roll-to-roll method. Throughput as high as 5 min/m^2 was achieved, thanks to the use of a kilowatt-level, tens of megahertz-class industrial femtosecond laser jointly with a polygon scanner delivering the beam at ≈100 m/s. Interestingly, a comprehensive set of mechanical tests and SEM analyses revealed, for the first time, that the forming process of metallic surfaces textured with LIPSS does not affect the material's mechanical properties or the surface morphology, that is, the surface functionality itself.

It can be asserted that if an untreated foil can undergo shaping, the same can be achieved after laser texturing. While additional research is needed to validate this conclusion for structures of micrometric size (DLIP, LDW) and thicker foils, we believe our findings pave the way to convert a laser-functionalised surface into a laser-functionalised product primed for industrial exploitation.

Author Contributions: Conceptualization, G.M.; Methodology, G.M. and S.R.; Validation, G.M.; Investigation, G.M., A.B., S.P., S.R. and M.K.; Resources, G.M.; Data curation, A.B., S.P. and S.R.; Writing—original draft, G.M., L.G., S.P. and S.R.; Writing—review & editing, G.M., L.G., S.P. and S.R.; Visualization, S.P., S.R. and M.K.; Supervision, G.M., P.K. and R.K.; Funding acquisition, G.M. All authors have read and agreed to the published version of the manuscript.

Funding: This research is part of "NewSkin" RIA and was funded by the Horizon 2020 Framework Programme (H2020) under grant agreement No. 862100.

Institutional Review Board Statement: Not applicable.

Informed Consent Statement: Not applicable.

Data Availability Statement: The data presented in this study are available on request from the corresponding author. The data are not publicly available due to privacy.

Acknowledgments: The authors thank Formplanet OITB and Carlos del Castillo from European Convention for Constructional Steelwork (ECCS).

Conflicts of Interest: Authors Sylwia Rzepa, Martina Koukolíková and Pavel Konopík were employed by the company COMTES FHT. The remaining authors declare that the research was conducted in the absence of any commercial or financial relationships that could be construed as a potential conflict of interest.

References

1. Mincuzzi, G.; Gemini, L.; Faucon, M.; Kling, R. Extending ultra-short pulse laser texturing over large area. *Appl. Surf. Sci.* **2016**, *386*, 65–71. [CrossRef]
2. Henriques, B.; Lasagni, A.F. Structuring Surfaces at the Speed of Light. *Biomed. Mater. Devices* **2023**. [CrossRef]
3. Hauschwitz, P.; Martan, J.; Bičišťová, R.; Beltrami, C.; Moskal, D.; Brodsky, A.; Kaplan, N.; Mužík, J.; Štepánková, D.; Brajer, J.; et al. LIPSS-based functional surfaces produced by multi-beam nanostructuring with 2601 beams and real-time thermal processes measurement. *Sci. Rep.* **2021**, *11*, 22944. [CrossRef] [PubMed]
4. Lasagni, A.F. How laser-based fabrication methods can be used to produce multifunctional surfaces. In Proceedings of the Laser Applications in Microelectronic and Optoelectronic Manufacturing (LAMOM) XXVII, San Francisco, CA, USA, 22–27 January 2022.
5. Grubert, N.; Hofmann, O.; Hesker, M.; Stollenwerk, J.; Holly, C. Beam shaping for large-area laser structuring in a roll-to-roll process. In *Novel Optical Systems, Methods, and Applications XXV*; SPIE: San Francisco, CA, USA, 2022.
6. Fraggelakis, F.; Mincuzzi, G.; Lopez, J.; Kling, R.; Manek-Hönninger, I. Controlling micron and submicron scale laser induced surface structures on stainless steel with industrial femtosecond lasers. *J. Laser Micro Nanoeng.* **2018**, *13*, 206–210. Available online: http://www.jlps.gr.jp/jlmn/assets/62ee6784438754e10e79608b3dc46d2e.pdf (accessed on 13 November 2023).
7. Mincuzzi, G.; Rebière, A.; Faucon, M.; Sikora, A.; Kling, R. Beam engineering strategies for high throughput, precise, micro-cutting by 100 W, femtosecond lasers. *J. Laser Appl.* **2020**, *32*, 042003. [CrossRef]
8. Lutey, A.H.; Lazzini, G.; Gemini, L.; Peter, A.; Onuseit, V.; Graus, J.; Fuso, F.; Kling, R.; Romoli, L. Insight into replication effectiveness of laser-textured micro and nanoscale morphology by injection molding. *J. Manuf. Process.* **2021**, *65*, 445–454. [CrossRef]
9. Cheng, Z.; Li, Y.; Xu, C.; Liu, Y.; Ghafoor, S.; Li, F. Incremental sheet forming towards biomedical implants: A review. *J. Mater. Res. Technol.* **2020**, *9*, 7225–7251. [CrossRef]
10. Emmens, W.; Sebastiani, G.; Boogaard, A.v.D. The technology of Incremental Sheet Forming—A brief review of the history. *J. Am. Acad. Dermatol.* **2010**, *210*, 981–997. [CrossRef]
11. Mincuzzi, G.; Bourtereau, A.; Sikora, A.; Faucon, M.; Kling, R. Pushing laser nano-structuring through mass production. In *Laser-Based Micro- and Nanoprocessing XVI*; SPIE: San Francisco, CA, USA, 2022.
12. Gronostajski, Z.; Pater, Z.; Madej, L.; Gontarz, A.; Lisiecki, L.; Lukaszek-Solek, A.; Łuksza, J.; Mróz, S.; Muskalski, Z.; Muzykiewicz, W.; et al. Recent development trends in metal forming. *Arch. Civ. Mech. Eng.* **2019**, *19*, 898–941. [CrossRef]
13. Raciukaitis, G. Ultra-Short Pulse Lasers for Microfabrication: A Review. *IEEE J. Sel. Top. Quantum Electron.* **2021**, *27*, 1–12. [CrossRef]
14. *ISO 6892-1:2021*; Metallic Materials—Tensile Testing—Part 1: Method of Test at Room Temperature. ISO: Geneva, Switzerland, 2021.
15. *ISO 1099:2017*; Metallic Materials—Fatigue Testing—Axial Force-Controlled Method. ISO: Geneva, Switzerland, 2017.
16. Zhang, Y.; Jiang, Q.; Long, M.; Han, R.; Cao, K.; Zhang, S.; Feng, D.; Jia, T.; Sun, Z.; Qiu, J.; et al. Femtosecond laser-induced periodic structures: Mechanisms, techniques, and applications. *Opto-Electron. Sci.* **2022**, *1*, 220005. [CrossRef]
17. Bonse, J.; Kirner, S.V.; Höhm, S.; Epperlein, N.; Spaltmann, D.; Rosenfeld, A.; Krüger, J. Applications of Laser-Induced Periodic Surface Structures (LIPSS). In Proceedings of the Laser-Based Micro- and Nanoprocessing XI, SPIE LASE, San Francisco, CA, USA, 31 January–2 February 2017. [CrossRef]
18. Bonse, J. Quo Vadis LIPSS?—Recent and Future Trends on Laser-Induced Periodic Surface Structures. *Nanomaterials* **2020**, *10*, 1950. [CrossRef] [PubMed]
19. Tsibidis, G.D.; Fotakis, C.; Stratakis, E. From ripples to spikes: A hydrodynamical mechanism to interpret femtosecond laser-induced self-assembled structures. *Phys. Rev. B* **2015**, *92*, 041405. [CrossRef]
20. Gnilitskyi, I.; Derrien, T.J.-Y.; Levy, Y.; Bulgakova, N.M.; Mocek, T.; Orazi, L. High-speed manufacturing of highly regular femtosecond laser-induced periodic surface structures: Physical origin of regularity. *Sci. Rep.* **2017**, *7*, 8485. [CrossRef] [PubMed]
21. Bonse, J.; Koter, R.; Hartelt, M.; Spaltmann, D.; Pentzien, S.; Höhm, S.; Rosenfeld, A.; Krüger, J. Femtosecond laser-induced periodic surface structures on steel and titanium alloy for tribological applications. *Appl. Phys. A* **2014**, *117*, 103–110. [CrossRef]

22. Sikora, A.; Faucon, M.; Gemini, L.; Kling, R.; Mincuzzi, G. LIPSS and DLIP: From hierarchical to mutually interacting, homogeneous, structuring. *Appl. Surf. Sci.* **2022**, *591*, 153230. [CrossRef]
23. Bauer, F.; Michalowski, A.; Kiedrowski, T.; Nolte, S. Heat accumulation in ultra-short pulsed scanning laser ablation of metals. *Opt. Express* **2015**, *23*, 1035–1043. [CrossRef]
24. Lopez, J.; Mincuzzi, G.; Devillard, R.; Zaouter, Y.; Hönninger, C.; Mottay, E.; Kling, R. Ablation efficiency of high average power ultrafast laser. *J. Laser Appl.* **2015**, *27*, 4906479. [CrossRef]
25. Jayanth, N.; Senthil, P.; Prakash, C. Effect of chemical treatment on tensile strength and surface roughness of 3D-printed ABS using the FDM process. *Virtual Phys. Prototyp.* **2018**, *13*, 155–163. [CrossRef]
26. Edwards, L.; Lyndon; Endean, M. (Eds.) *Manufacturing with Materials*; Butterworth-Heinemann: Oxford, UK, 1990; Volume 355.
27. Lee, S.; Pegues, J.W.; Shamsaei, N. Fatigue behavior and modeling for additive manufactured 304L stainless steel: The effect of surface roughness. *Int. J. Fatigue* **2020**, *141*, 105856. [CrossRef]
28. Parareda, S.; Frómeta, D.; Casellas, D.; Sieurin, H.; Mateo, A. Understanding the Fatigue Notch Sensitivity of High-Strength Steels through Fracture Toughness. *Metals* **2023**, *13*, 1117. [CrossRef]
29. San-Blas, A.; Martinez-Calderon, M.; Buencuerpo, J.; Sanchez-Brea, L.; del Hoyo, J.; Gómez-Aranzadi, M.; Rodríguez, A.; Olaizola, S. Femtosecond laser fabrication of LIPSS-based waveplates on metallic surfaces. *Appl. Surf. Sci.* **2020**, *520*, 146328. [CrossRef]
30. Yang, Z.; Zhang, J.; Li, S.; Li, G.; Wang, Q.; Hui, W.; Weng, Y. On the critical inclusion size of high strength steels under ultra-high cycle fatigue. *Mater. Sci. Eng. A* **2006**, *427*, 167–174. [CrossRef]
31. Gräf, S.; Kunz, C.; Undisz, A.; Wonneberger, R.; Rettenmayr, M.; Müller, F.A. Mechano-responsive colour change of laser-induced periodic surface structures. *Appl. Surf. Sci.* **2018**, *471*, 645–651. [CrossRef]